

Electrical Impedance Tomography of Known Targets

Abelardo Ramirez¹, William Daily¹, Andrew Binley², and Douglas LaBrecque³
Lawrence Livermore National Laboratory, Livermore Calif.¹, Lancaster University,
Lancaster, U.K.², Steamtech, Inc., Bakersfield, Calif.³

ABSTRACT

Electrical impedance tomographs (showing magnitude and phase) of known, laboratory-scale targets are reported. Also presented is a generalization of a proven electrical resistance tomography (ERT) algorithm, to account for electrical impedance. Three methods are used to reconstruct electrical impedance data and their results compared. The first two methods employ approximate relationships between the measurements and reconstructed tomograph while the third approach employs fully complex algebra to account for the real and imaginary components of electrical impedance data.

The electrical impedance tomography (EIT) and the perturbation analysis (PA) algorithms provided useful magnitude and phase images for the frequency range of 0.0625 to 64 Hz; images for 256 and 1024 Hz are also presented but these were not reliable. The frequency effect (FE) approach did not produce reliable phase images. Comparisons of the ERT and EIT magnitude images show that both methods provided equivalent results for the water blank, copper rod and PVC rod targets. The EIT magnitude images showed better spatial resolution for the sand-lead mixture target. Phase images from both methods located reasonably well anomalies of both high and low contrast induced polarization (IP) and provided better spatial resolution than the magnitude images. When IP was absent from the data, the EIT and PA algorithms reconstructed phase values consistent with the data noise levels.

Introduction

There is a rich literature generated in the early and mid 1900's on the measurement and interpretation of induced polarization (IP) because of its role in the mining industry (*e.g.*, Marshall and Madden, 1959; Zonge and Wynn, 1975; Sumner, 1976; Bertin and Loeb, 1976). Large ore bodies were known to have uniquely large IP effects, easily measured for exploration and characterization of the deposits for mining. More recently, geophysicists have turned their attention to using IP effects to map ground water organic contamination or petroleum reservoirs, since it has been shown that some clay-organic reactions produce unique low frequency electrical spectra (*e.g.*, Olhoeft, 1985; Borner *et al.*, 1993).

Previous reports describing methods to invert resistivity and IP data include Pelton *et al.*, (1978), LaBrecque *et al.*, 1994, and Oldenburg and Li (1994), and Kemna and Binley, 1996. Other reports describe tomography of only resistivity (*e.g.*, Ramirez *et al.*, 1996). The work reported herein is an attempt to generalize the inversion of resistivity imaging or electrical resistance tomography (ERT) as defined by LaBrecque *et al.* (1996a) to include imaging of the reactive (IP) component of the earth's response as well.

Induced Polarization in Geophysics

There are many excellent reviews of IP theory and practice in geophysics which need not be duplicated here

(*e.g.*, Marshall and Madden, 1959; Zonge and Wynn, 1975; Vinegar and Waxman, 1984; Van Voorhis *et al.*, 1973; Shuey and Johnson, 1973; Pelton *et al.*, 1983; Pelton *et al.*, 1984; Wynn and Zonge, 1975). However, it is useful to review briefly some of the key ideas as they pertain to inversion of electrical impedance data, interpretation of the resulting images and the relation of these to current geophysical practice.

When a voltage impressed on earth materials is terminated, the resulting current does not abruptly end but decays much like that from a charged capacitor discharging through a resistor. The same phenomenon is manifested in the frequency domain as a frequency dependent resistance and a phase lag between the current and the impressed voltage. In the terminology of electrical engineering, an impedance consists of both magnitude and phase (the magnitude indicates the amplitude of the resistance and a non-zero phase angle indicates a capacitive or inductive reactance in the system). In the terminology used in geophysics, the magnitude of the complex impedance is the resistance and the phase shift is related to chargeability, the unit of measure for IP in the time domain. The time domain and frequency domain descriptions are equivalent when the phenomenon are linear, being Fourier transform pairs. In this work, the frequency domain approach will be used. Both data and inversion results will be expressed as magnitude (also referred to as resistivity in this paper) and phase at several discrete frequencies.

Marshall and Madden (1959) point out that IP can be thought of as a manifestation of energy stored in the medium which is released after the driving voltage is terminated. There are many mechanisms which may be responsible for this energy storage: metallic polarization, electromagnetic induction effects, electrokinetic, thermoelectric, and membrane polarization.

Metallic polarization (electrode polarization) results when electrical current flows across a metal-electrolyte interface. Electrochemical barriers to current flow exist because current continuity at the boundary requires electronic conduction in the metal to match ionic conduction in the electrolyte. These barriers behave like an impedance which is in series with the impedance of the electrode and that of the bulk rock. This interface impedance is sometimes called contact impedance and it typically decreases with frequency. The additional voltage required to overcome these electrochemical barriers is called the overvoltage. On a macroscopic scale, the phenomenon exists at measurement electrode surfaces and microscopically it is responsible for the IP response of mineralized ore bodies (Van Voorhis *et al.*, 1973). As will be shown later, this mechanism is responsible for one of the IP sources studied in the present analysis.

Membrane polarization results when cations are selectively bound to zones (the 'membrane zone') along the pore walls where minerals with significant cation exchange capacity (*e.g.*, clay minerals) are located. An external voltage gradient causes displacement of cations in the zone. The anion concentration is also unbalanced to maintain neutrality, but when the external voltage vanishes, the resulting gradients will modify the ion flow until a balance is reached. Although this is an important source of IP in natural systems, the physical scale models used in this work probably do not generate significant membrane polarization.

Marshall and Madden (1959) also describe how the electrokinetic and thermoelectric effects can produce IP, but they calculate very small polarizations and conclude that these are usually not important mechanisms. They also include electromagnetic induction (also known as electromagnetic coupling; see Wynn and Zonge, 1975) as a source for IP, since it meets the broad definition as an energy storage mechanism. Electromagnetic coupling should be unimportant for the cases discussed here because of the low frequency range used (below 1024 Hz) and short distances.

Olhoeft (1985) adds to the IP mechanisms list inorganic reactions which involve chlorinated compounds reacting with clay minerals. This mechanism has received attention recently because of the possibility of using the unique nature of this effect for locating chlorinated contaminants in soils and groundwater (Olhoeft, 1985, Vanhala *et al.*, 1992, Borner *et al.*, 1993, Daily *et al.*, 1998). However,

these mechanisms are not expected to be important in the scale model data used here.

Electrical Impedance Tomography

Electrical resistance tomography (ERT) was proposed independently by Henderson and Webster (1978) as a medical imaging tool and by Lytle and Dines (1978) as a geophysical imaging tool. The technique has been actively developed for medical imaging (*e.g.*, Isaacson, 1986; Barber and Seager, 1987; Yorkey *et al.*, 1987). Early adaptations of the technique to the field of geophysics were by Pelton *et al.*, (1978), Dines and Lytle (1981), Tripp *et al.* (1984), Wexler *et al.*, (1985). Recent developments are discussed by Ellis and Oldenburg (1994), Oldenburg and Li (1994), Sasaki (1992), Daily and Owen (1991), Zhang *et al.* (1995), and Shi *et al.* (1996). The geophysical community has also found the technology of practical value, so that what were once research tools are now becoming commercially available.

Published efforts to image both the magnitude and phase of the measured impedance (EIT) have been few and have generally relied on a linear approximation such as that by Seigel (1959) which requires a knowledge of the DC resistivity distribution (*e.g.*, Oldenburg and Li, 1994). Recent algorithms which also solve the EIT inversion problem can be found in Weller *et al.* (1996), Yuval and Oldenburg (1997) and in Shi *et al.* (1998).

The purposes of the work presented here are to: 1) describe and evaluate a rigorous inversion of electrical impedance using an algorithm which solves the forward and inverse problems using complex algebra to account for both the resistive and reactive nature of the current flow, and 2) compare results from this rigorous method to that obtained from two approximate methods. Laboratory-scale targets having known location, size, and IP response were used to provide data for these evaluations.

Our principal interest is geophysical applications. Therefore, the input frequency is limited to the range 0.0625 to 1024 Hz in order to minimize problems with cable to cable coupling and cable stray capacitance. The survey geometry used is typical of cross borehole surveys. It is beyond the scope of this project to address electrode arrangements and frequencies which would be more applicable for applications such as medical imaging or nondestructive evaluation.

Theory

Ohm's law states that the electrical potential difference between two electrodes is linearly related to current with the impedance ρ^* (* denotes complex term) as the proportionality factor. Because the potential and current

may be out of phase, the resistivity must be represented as a complex quantity or impedance.

The goal is to calculate the impedance distribution which is consistent with impedance magnitude and phase measurements made on the boundary of a region. Three different methods for solving this inverse problem are presented and applied here. Two of the methods are approximate and were chosen because they have been used in the past by IP investigators to image the phase or IP response. The first approximate method is based on the fact that changes in impedance magnitude with frequency are related to the phase. This so called frequency effect (FE) (Shuey and Johnson, 1973 and Van Voorhis *et al.*, 1973) can be used to estimate the phase response by comparing impedance magnitude at two frequencies. The second approximate method is based on the linear approximation proposed by Seigel (1959), which assumes that the chargeability of a body alters its effective resistivity so that a two step process can be used in which the impedance magnitude (resistance) is first calculated and then the reactance is calculated as a perturbation consistent with the measured chargeability or phase. The third approach solves the forward and inverse problems in the complex plane, and thus rigorously relates the measured and inverted impedances.

Frequency Effect (FE)

The FE approach takes advantage of the fact that IP causes a frequency dependent resistivity (magnitude of the impedance) (Shuey and Johnson, 1973; Pelton *et al.*, 1984). These authors point out that rocks only exhibit relaxation behavior. This implies that rocks exhibit only capacitive reactances. Normally, the physical mechanisms of electrical relaxation are such that the magnitude of the impedance decreases with frequency. This fact is exploited by the approach we will explore below.

Assuming a constant phase angle with changing frequency, a universal relationship between FE and phase can be established (Pelton *et al.*, 1984). FE is defined as:

$$FE = [\rho(\omega) - \rho(A\omega)]/\rho(\omega) \quad (1)$$

where $\rho(\omega)$ is the magnitude of the resistivity ($\rho = |\rho^*|$) at frequency ω and A specifies the frequency separation between the two measurements. Pelton *et al.* (1984), point out that the FE measurement is an attempt to specify the slope on a double logarithmic plot by taking the first backward difference. They show the relationship between the FE and phase as:

$$\phi = a\pi/2 \quad (2)$$

where ϕ is the phase in radians at the geometric mean frequency $A^{1/2}\omega$, and $a = -\log(\rho(\omega)/\rho(A\omega))/\log(A)$.

There are several literature reports indicating that resistivity changes based on ERT tomographs have been used successfully to image subsurface time-dependent processes

(e.g., Daily *et al.*, 1992; LaBrecque *et al.*, 1996b; Ramirez *et al.*, 1995). The reports indicate that this approach was used to map a variety of subsurface processes such as water infiltration, leaks from tanks, air sparging, and steam floods. These resistivity change tomographs were calculated using results produced by the ERT algorithm described in the next section. Equations 1 and 2 suggest that FE could be used to produce images of subsurface reactance if one could produce resistivity images using an ERT algorithm, not as a function of time but rather as a function of frequency. That is, a resistivity tomograph is produced using data at one frequency, and a second tomograph is computed using data collected at a different frequency. The two tomographs are combined on an element by element basis as indicated by Eqs. 1 and 2, thereby producing a phase tomograph. The validity of this approach will be explored in a subsequent section.

Numerical Inversion

DC Resistivity

The ERT algorithm uses a modified Marquardt algorithm to iteratively solve the regularized (Tikhonov and Arsinen, 1977) nonlinear resistivity (ERT) problem. de-Groot-Hedlin and Constable (1990) describe a similar algorithm to the one described below, but our implementation of the Occam's inversion is somewhat different.

Both the nonlinear resistivity or linear approximation to the IP problem can be written as

$$\underline{WD} = \underline{W} \cdot \underline{F}(\underline{P}), \quad (3)$$

where \underline{D} is the vector of known data values, \underline{W} is a weighting matrix, \underline{P} is the vector of unknown parameters, and $\underline{F}(\underline{P})$ is the forward solution. In the resistivity problem, each parameter consists of the natural logarithms of the conductivities of the elements in the finite element mesh within a rectangular block of elements. For IP, each parameter is a rectangular block of element IP parameters.

The inverse algorithm iteratively finds the maximum value of α , the stabilization parameter, for which minimizing the objective function,

$$\Psi(\underline{P}) = \chi^2(\underline{P}) + \alpha \Omega(\underline{P}), \quad (4)$$

gives a value of $\chi^2(\underline{P})$ equal to an apriori value; typically $\Omega(\underline{P})$ is chosen so that $\chi^2(\underline{P})$ equals the number of data points. In Eq. 4, $\Omega(\underline{P})$ is the stabilizing function (Tikhonov and Arsinen, 1977), and χ^2 is the chi-squared statistic which is given by

$$(\underline{D} - \underline{F}(\underline{P}))^T \underline{W} (\underline{D} - \underline{F}(\underline{P})) = \chi^2. \quad (5)$$

Although there are several choices for $\Omega(\underline{P})$, the results below use the form

$$\Omega(\underline{P}) = \underline{P}^T \underline{R} \underline{P} \quad (6)$$

where $\underline{\mathbf{R}}$ is the roughness matrix which has the form of the 2-D Laplacian operator (Sasaki, 1992). The roughness matrix $\underline{\mathbf{R}}$ is constructed from

$$\underline{\mathbf{R}} = \underline{\mathbf{x}}^T \underline{\mathbf{x}} + \underline{\mathbf{z}}^T \underline{\mathbf{z}}, \quad (7)$$

where $\underline{\mathbf{x}}$ and $\underline{\mathbf{z}}$ are matrices, each row of which contains the first order differences operators in the X and Z directions respectively.

For resistivity, the first step in the iterative process to determine \mathbf{P} is to approximate the non-linear resistivity forward problem via the first-order terms of a Taylor's series

$$\mathbf{F}(\mathbf{P}) \approx \mathbf{F}(\mathbf{P}_i) + \mathbf{A}(\mathbf{P} - \mathbf{P}_i). \quad (8)$$

In equation (8), \mathbf{P}_i is the vector of estimated parameters at the i th iteration and \mathbf{A} is the sensitivity matrix also at the i th iteration and has elements, $a_{j,k}$,

$$a_{j,k} = \frac{\partial}{\partial p_k} \mathbf{F}_j(\mathbf{P}_i), \quad (9)$$

where p_k is the k th element of \mathbf{P}_i and \mathbf{F}_j is the forward solution corresponding to the j th data point.

The first step in each Marquardt iteration is to find α . To do this, we use a root finding algorithm from Press *et al.* (1986) to find the maximum value of alpha for which

$$(\mathbf{D} - \underline{\mathbf{A}}_{i-1} \mathbf{P})^T \underline{\mathbf{W}}^T \underline{\mathbf{W}} (\mathbf{D} - \underline{\mathbf{A}}_{i-1} \mathbf{P}) = \chi^2 \text{ apriori}, \quad (10)$$

where \mathbf{P} is given by

$$\begin{aligned} \mathbf{P} = & \mathbf{P}_{i-1} + (\underline{\mathbf{A}}_{i-1}^T \underline{\mathbf{W}}^T \underline{\mathbf{W}} \underline{\mathbf{A}}_{i-1} + \alpha \underline{\mathbf{R}})^{-1} \\ & \times (\underline{\mathbf{A}}_{i-1}^T \underline{\mathbf{W}}^T \underline{\mathbf{W}} (\mathbf{D} - \mathbf{F}(\mathbf{P}_{i-1})) + \alpha \underline{\mathbf{R}} \mathbf{P}_{i-1}), \end{aligned} \quad (11)$$

and \mathbf{P}_{i-1} is the parameter vector from the previous iteration or from an initial guess. Thus, Eq. 11 solves the local linear approximation to the resistivity which gives a local approximation to α .

For the resistivity problem, the parameters are found using an algorithm similar to that described by Bard (1974). The estimate of the parameter vector, \mathbf{P}_i is:

$$\begin{aligned} \mathbf{P}_i = & \mathbf{P}_{i-1} + s(\underline{\mathbf{A}}_{i-1}^T \underline{\mathbf{W}}^T \underline{\mathbf{W}} \underline{\mathbf{A}}_{i-1} + \lambda \underline{\mathbf{I}} + \alpha \underline{\mathbf{R}})^{-1} \\ & \times (\underline{\mathbf{A}}_{i-1}^T \underline{\mathbf{W}}^T \underline{\mathbf{W}} (\mathbf{D} - \mathbf{F}(\mathbf{P}_{i-1})) + \alpha \underline{\mathbf{R}} \mathbf{P}_{i-1}), \end{aligned} \quad (12)$$

where λ is the Marquardt multiplier, $\underline{\mathbf{I}}$ is the identity matrix and s is the step length. λ serves to stabilize the iterative inverse process as the step length is adjusted, but it does not directly affect the inverse solution. The iterations are repeated until χ^2 equals χ^2 apriori and α converge to a constant value.

Perturbation Analysis (PA)

An alternative to the FE approach is to use a linear approximation based on the work of Seigel, 1959. This linearized perturbation analysis (PA) is one of the methods used here to invert IP data. Note that for IP, we often use

the terms percent frequency effect (PFE), chargeability or phase lag to describe the material properties, and the quantities measured by geophysical instruments. The method described in this section is very similar to the algorithm described by Oldenberg and Li (1994 who provide a detailed description. Below we summarize the key concepts.

Seigel (1959) showed that apparent chargeability η_a , (the time-domain IP measurement) can be calculated as small perturbations of region resistivities as long as the intrinsic IP effects are small (much less than 1) and the IP problem is approximately linear. He also showed that, for small IP, the chargeability sensitivity is equivalent to the DC resistivity sensitivity.

The PA method involves a two step process. First, the electric potentials are inverted to recover a background conductivity using equations 11 and 12 above. Following Siegel's approach, the effect of chargeability on the ground can be modeled by using the DC resistivity forward operator but with the conductivity σ replaced by:

$$\sigma = \sigma(1 - \eta) \quad (13)$$

where η is the chargeability, and $\eta \ll 1$. As shown by Oldenberg and Li (1994), η can be computed by carrying out two DC resistivity forward models with conductivities σ and $\sigma = \sigma(1 - \eta)$:

$$\eta_a = \frac{F[\sigma(1 - \eta)] - F[\sigma]}{F[\sigma(1 - \eta)]} \quad (14)$$

where F is the forward mapping operator used in the DC resistivity case and η_a is the apparent chargeability.

The third IP measure, phase lag, can also be modeled as a linear perturbation of the form of Eq. 14. For frequency domain data we will redefine η as:

$$\eta = \frac{\nu - \nu(\cos(\phi))}{\nu} = 1 - \cos(\phi) \quad (15)$$

where ν is the potential measured at DC and ϕ is the phase angle. Note that for small phase angles yield values between 0 and 1 and $\eta \ll 1$. Equation 14 is then used to solve the forward IP problem.

Once an adequate value has been found for α during DC resistivity inversion, the IP problem, since it is assumed linear, is solved in one iteration. The inverse solution is implemented by linearizing Eq. 14. Oldenberg and Li (1994) showed that this linearization yields:

$$\eta_a = -\sum_j \frac{\partial \ln \nu}{\partial \ln \sigma_j} \eta_j \quad (16)$$

Fortunately, the partial derivatives with respect to the logarithm of conductivity shown in Eq. 16, are calculated as part of the DC resistivity inversion process as discussed in the previous section. Thus, relatively little added computational effort is required to calculate IP values.

Electrical Impedance Tomography (EIT)

We now describe our approach to generalize the ERT algorithm described by LaBrecque *et al.* (1996a) to allow for the reactive response of the system (further details may be found in Kemna and Binley, 1996).

To formulate the forward problem, we assume that the region of interest may be represented as a two-dimensional impedance distribution, ρ^* . If electromagnetic effects can be neglected, the forward problem is defined by the Fourier transformed Poisson's equation for a point source with real current

$$\frac{\partial}{\partial x} \left(\frac{1}{\rho^*} \frac{\partial v^*}{\partial x} \right) + \frac{\partial}{\partial z} \left(\frac{1}{\rho^*} \frac{\partial v^*}{\partial z} \right) - \lambda^2 \frac{v^*}{\rho^*} = -I\delta(x)\delta(z) \quad (17)$$

Here, v^* is the transformed complex potential and λ is the transformation variable. This differential equation may be solved using the finite element method for given boundary conditions. Inverse Fourier transform and appropriate superposition of the calculated potentials yields the complex transfer resistance of an arbitrary electrode configuration in the considered plane, from which an apparent conductivity can be calculated.

To solve the inverse problem, due to a possibly wide range of impedances, it is common to use log transformed parameters, that is, $P_j^* = -\ln(\rho_j^*)$ ($j = 1, 2, \dots, M$) as the parameters of the inversion, where ρ_j^* are the complex resistivities of one or more elements depending on the parameterization and, M is the number of parameters. Note that the complex logarithm separates the real logarithm of magnitude and phase of its argument into real and imaginary parts.

The objective function minimized here consists of the data misfit (with F as the operator of the forward solution, as before) and the model roughness (as used for numerous ERT inversion algorithms, see for example Eqs. 8 and 9):

$$\psi(p^*) = [D^* - F^*(P^*)]W^T W[D^* - F^*(P^*)] + \alpha P^{*T} R P^* \quad (18)$$

where D^* are the measured complex resistances, and as before, $F^*(P^*)$ are the corresponding forward model resistances due to parameters P^* , W is a vector of standard deviations of the data used to weight individual measurements, R is a roughness matrix used to force smoothing of the resistivity distribution and stabilize the inverse solution and α is a smoothing parameter.

Minimization of the objective function in Eq. 18 is achieved through an iterative solution. The procedure terminates when the desired data misfit has been reached. The approach is similar to that originally employed by deGroot-Hedlin and Constable (1990). The inversion process excludes solutions where the P^* have positive phase angles.

The objective function in the form of Eq. 18 is real even though the data, model and parameters are complex

terms. This formulation imposes restrictions on assignment of complex weights since the product $W^T W$ is also real. Consequently, it is impossible to separate errors in magnitude and phase in the weighting process. This could be achieved by decoupling the real and imaginary components; this approach may be the logical extension of this work. Our objective here, however, is to explore the possible benefits (if any) of a fully complex inversion of EIT data in comparison to more conventional procedures such as PA and FE.

Experimental Procedure

The various inversion schemes can be evaluated using synthetic or measured data. Typical of the first approach is to calculate the data by solving Poisson's equation for a given impedance distribution, add some type of random signal to simulate measurement error, invert the result, and compare the model and result for correspondence. This approach has the advantages that it is fast and relatively easy to implement, but has several drawbacks. We believe that the most serious drawback is the simulation of measurement error.

Iterative algorithms which rely on stabilized objective function minimization to solve the inverse problem can be very sensitive to the actual data error as well as to erroneous estimates of that error. In fact, LaBrecque *et al.* (1996a) have pointed out that it can be more important to know the data errors than to have small errors. Clearly, if the errors in the measurements were known, then it would be a simple matter to remove them from the measurements to get the true values. However, we are forced to estimate individual errors or assign statistical properties to the errors of large data sets because we can never know exactly the error of any single measurement.

A typical approach used with field data assumes that the noise is random and Gaussian. Based on these assumptions, one hopes to estimate the characteristics of that model by repeating the measurement. Years of resistivity measurements in the laboratory and field indicate to us that measurement error is neither random nor Gaussian (Iwatate *et al.*, 1996) and that it is not possible to formulate a realistic numerical model that simulates observed measurement errors. Without a good noise model, synthetic data can not be made to simulate real measurements.

Given that data errors are so important to the inversion process, we have chosen to study the behavior of the methods of interest using scale model data collected on known targets, and the same data acquisition system and approach used for field measurements. We believe that the results from such a test are more informative than results from synthetic data because the scale model test replicates more realistically the noise environment likely to be present during field deployments. Also, the scale model tests pro-

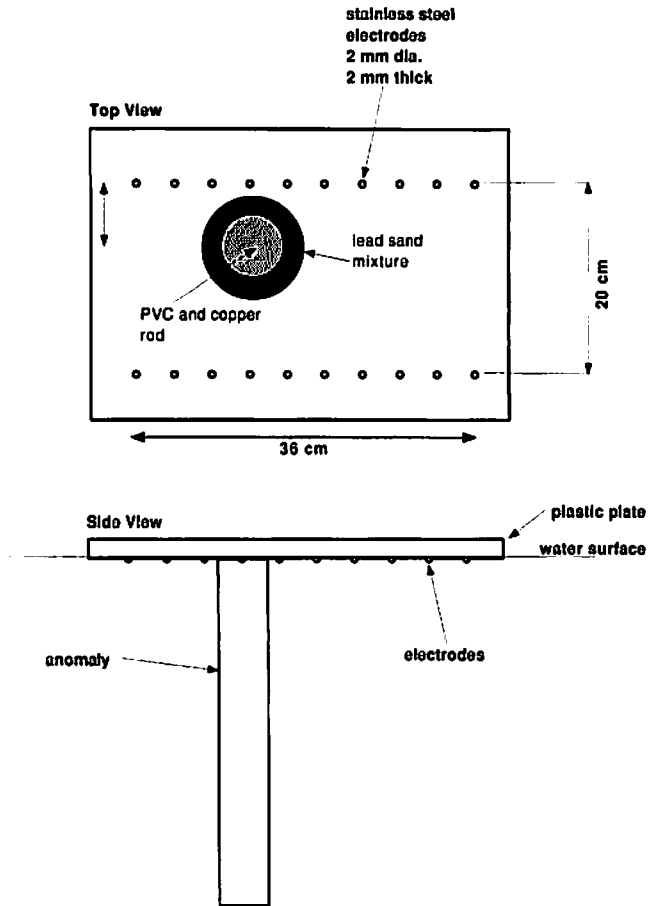


Figure 1. Experimental arrangement of the scale model used. Two rows of 10 stainless steel electrodes models a cross-borehole scheme. The setup exploited symmetry and allowed current flow only in a half space. Position and size of the target are shown to scale. The water tank walls are more than 10 dipole lengths from the region of interest.

vide data from continuous media and thus allow algorithm evaluation with realistic discretization error. These errors are related to the size and number of mesh elements used to represent the continuous medium in which the measurements are made.

Water Tank Setup

The scale model used reproduced the sampling geometry typical of geophysical electrical imaging. Twenty electrodes were arranged, as shown in Fig. 1, in two columns of 10 to simulate the arrangement typical of cross borehole imaging. The electrode arrays were mounted on one side of a plastic plate which was placed horizontally at the surface of the water. Anomalies were attached to the plastic plate to hang between the electrode arrays in the uniformly conductive water. The fiberglass water tank was 3.1 meters in diameter and 2.45 meters deep. The tank was

large relative to the electrode array dimensions to eliminate significant effects in the measurements from the tank walls.

Each data set consisted of 170 linearly independent measurements (plus a full set of reciprocal measurements). A dipole-dipole survey approach was used to collect the data. The ratio of each voltage to the corresponding current is a (complex) transfer impedance consisting of a magnitude and phase. Data were acquired at 8 frequencies: 0.0625, 0.25, 1.0, 4.0, 16, 64, 256 and 1024 Hz on each of 4 resistivity scale models. The four resistivity models used were:

Model 1. No target present; this model will be referred to as the “water blank” model. Water of uniform resistivity was the target. The purpose of this model was to determine the response of the inversion algorithm to a uniform impedance distribution (32 ohm-m) with no reactive part (phase angle equal to zero). This data was used also to generate the error estimates discussed below.

Model 2. Metallic target; this model will be referred to as the “copper rod” model. A 6.7 cm diameter PVC pipe wrapped with copper tape was placed in the water with its long axis perpendicular to the plane of the electrodes. This two-dimensional model tested the inversion algorithm with a conductive anomaly of relatively high contrast relative to the background water and a relatively large reactive component. The reactive component was due to the mechanism of electrode polarization at the copper-water interface (Van Voorhis *et al.*, 1973).

Model 3. Plastic target; this model will be referred to as the “PVC rod” model. A 6.7 cm diameter PVC pipe was placed in the water below the image plane with its long axis perpendicular to the plane of electrodes. This two-dimensional model tested the inversion algorithm with a resistive anomaly of high contrast relative to the background but with no reactive component.

Model 4. Intermediate contrast target; this model will be called the “sand-lead” model. A cloth bag containing a mixture of sand and lead shot (2 parts sand and 1 part by volume of no. 7.5 lead shot) approximately 11 cm in diameter and 17 cm long was placed in the image plane below the plastic plate. This model provided a target of intermediate resistivity and IP contrast relative to the other targets used. A small reactive component was expected because of the change from electrolytic to electronic conduction occurring at the surface of each piece of lead shot.

The finite element mesh used to represent the region consisted of 30 elements across by 38 elements down. The region between the electrodes was discretized using 10 elements across and 18 elements down.

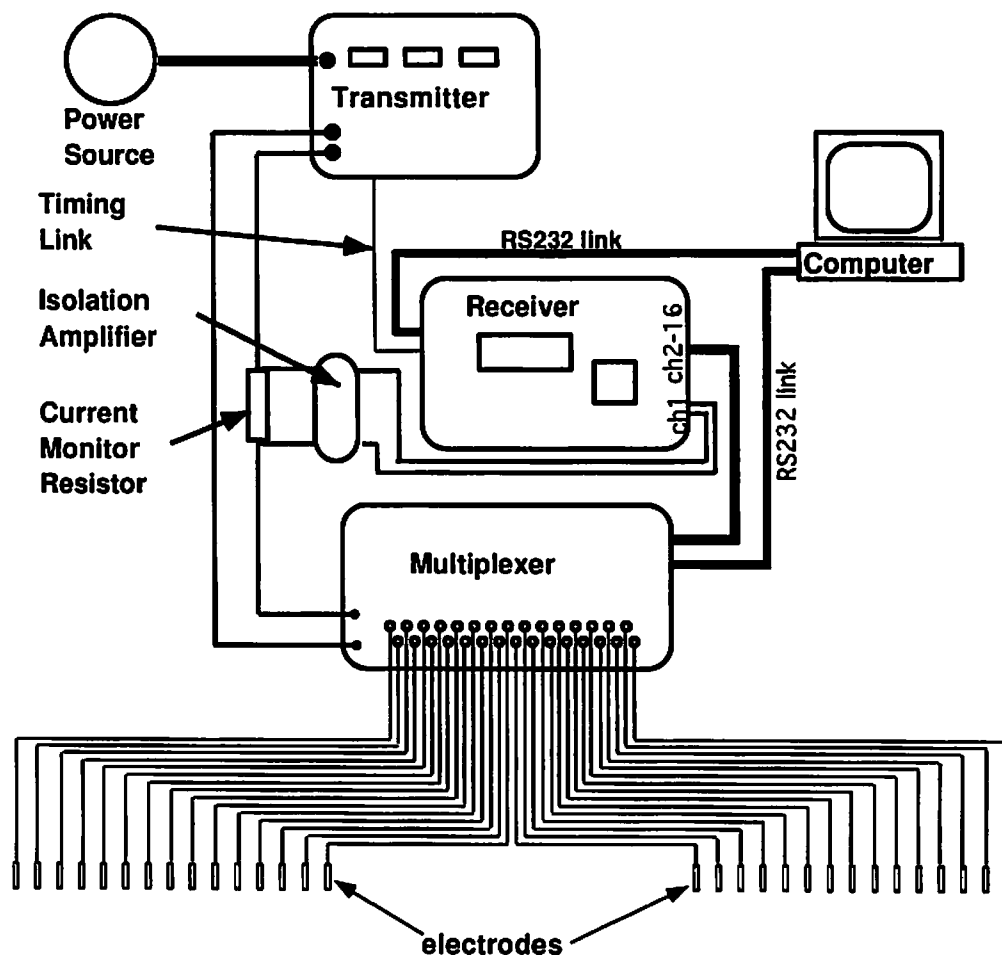


Figure 2. Block diagram of the data acquisition system. Each of the 10 receiver channels was multiplexed to the 20 electrodes for all the linearly independent, 4 electrode dipole-dipole data. The source current was monitored as a voltage across a calibrated resistor. System control and data recording were performed under computer control.

Data Acquisition System

The data acquisition system consisted of a transmitter or current source, a receiver which measured the transmitted current as well as the resulting electrode potentials, a multiplexer for connecting the electrodes to the transmitter and receiver, and a computer for system control and data archival. A block diagram of the system is shown in Fig. 2.

The heart of the system is a multichannel detector capable of supporting up to 16 modular receivers, each with a 10 M ohm input impedance at DC, a 16-bit A/D converter and a dynamic range from $\pm 0.03 \mu\text{V}$ to $\pm 32 \text{ V}$. There is an automatic SP offset adjustment of up to $\pm 2.25 \text{ V}$ in $65 \mu\text{V}$ steps. The receiver operated in the frequency domain.

Switching between electrodes was accomplished at a central multiplexer which can address up to 30 separate electrodes and allowed for complete freedom in specifying which electrodes are used for the current source and which are used for potential measurement.

Data Accuracy

Accuracy is usually defined as "the conformity of an indicated value to an accepted standard value, or true value" (precision, on the other hand, is the "degree of exactness with which a quantity is stated") (Considine, 1983). As one measure of system accuracy, we have performed a simple system calibration against a known impedance standard. One channel was used to measure the current through a standard resistor while another channel was used to measure the resulting potential drop across the resistor. Typical magnitude calibration was significantly better than 1%.

A significant level of effort was undertaken in order to improve the accuracy of the phase angles measured. Early on, it was discovered that attenuators in the receiver as well as large stray capacitance generated in the multiplexer were responsible for large phase angle errors. These errors were greatly mitigated by: 1) modification of the multiplexer electronics, 2) insuring that attenuators in the re-

ceiver were not used, and 3) by implementing a calibration procedure which used measurements on pure resistances (0 phase angles) to automatically remove any remaining phase shifts caused by the electronics.

Unfortunately, this calibration only produces a lower limit of data error because electrode noise, cable coupling, electromagnetically coupled external noise sources, etc. will combine to increase the errors. Maximizing data accuracy is difficult on a system where errors may vary from one electrode pair to another, or even change with time. Equally important, but just as difficult to obtain, is a reliable *measure* of accuracy.

Several measures are typically used to estimate data quality. One of the most common is repeatability. Our experience has been that repeatability leads to a serious underestimate of error. We have found that reciprocity is a better estimate of error (for a 4 electrode measurement of transfer impedance, the reciprocal is found by interchanging the current source and potential measurement dipoles).

Figure 3 shows reciprocal difference data collected using the water blank model. The survey conditions were as close as possible to those of the other model anomalies: same electrodes, same measurement system, same measurement sampling protocol, same frequencies, etc. Given that tap water should not generate a reactive component, the normal and reciprocal magnitudes from the corresponding electrode pairs should be identical at each frequency and the phase angles should equal zero. The actual error in transfer impedance magnitude is estimated by

$$|R_n - R_r| \quad (19)$$

which is plotted against R_n , where R_n is the magnitude of the normal transfer impedance and R_r is the magnitude of the corresponding reciprocal transfer impedance. Phase errors could be estimated by comparing the normal and reciprocal phases or by comparing either to zero. We have chosen to plot

$$|\phi_n - \phi_r| \quad (20)$$

against ϕ_n , where ϕ_n is the normal phase and ϕ_r is the reciprocal phase (phase angles have been unwrapped so that all angles are in the first or fourth quadrants). Error-free data would plot along the abscissa of the magnitude plots and at the origin of the phase plots because there are no anomalies to cause phase delays.

Based on our experience, the data represented in Fig. 3 are comparable with good field data. The magnitude errors are predominantly less than 1% of the measured values. Likewise, the phase errors are small, predominantly less than 5 milliradians at frequencies below 64 Hz.

The magnitude and phase errors show interesting trends. There is a minimum error in the magnitudes of a few tens of milliohms at 16 Hz. The magnitude errors increase to a few thousand milliohms at the low frequencies

and a few hundred milliohms at the high frequency. For frequencies equal to and higher than 4 Hz, a one second integration time was used (*e.g.*, for 16 Hz, 16 cycles were averaged together). Below 4 Hz only 2 cycles were averaged and this may explain the larger low frequency errors. The main source of errors at 1024 Hz is likely due to measurement electronics effects which were not completely removed by the system calibration. Notice that, for all frequencies, there is no clear correlation between magnitude and its estimated error. A popular error model which assumes that data noise is proportional to the magnitude value does not fit these data.

The phase errors are consistently less than about 5 milliradians (0.29 degrees) below 64 Hz but above this frequency there is a sharp increase in error. At 1024 Hz, most phases are below 100 milliradians but some are as much as 300 milliradians. These errors may result from effects of stray capacitance, which becomes more troublesome with increasing frequency.

Test results suggest that the stainless steel electrodes used for this work, although not perfect, have a relatively small polarizability. Measurements made on a carbon resistor, which removed any reactive effects due to electrode polarization but left other electronic sources of phase errors, resulted in phase angles errors of 50 to 100 milliradians at 1024 Hz. This residual phase error is probably caused by amplifiers, cable capacitance and other specifics of the measurement system. These error sources are also present during field surveys and we are forced to accept both electrode and electronics errors. The errors shown in Fig. 3 were used to define the data weighting vector in Eq. 18.

Results and Discussion

Data were collected on the four different targets described above using water as a medium of known and uniform resistivity (32 ohm-m). The results are displayed in Figs. 4 through 6.

Frequency Effect Analysis

Figure 4 shows the phases obtained using the frequency effect (FE) approximation. The phase images were produced by comparing the magnitudes reconstructed with the ERT algorithm, for each of two frequencies as indicated by equations 1 and 2. The frequencies compared were different by a factor of 16. The frequencies shown at the top of the figure represent the geometric mean of the two frequencies used in the comparison (the 0.25 Hz tomograph was calculated using the magnitudes obtained at 0.0625 and 1 Hz, the 1 Hz tomograph was calculated using the magnitudes obtained at 0.25 and 4 Hz, the 4 Hz tomograph was calculated using the magnitudes obtained at 1 and 16 Hz, the 16 Hz tomograph was calculated using the magnitudes

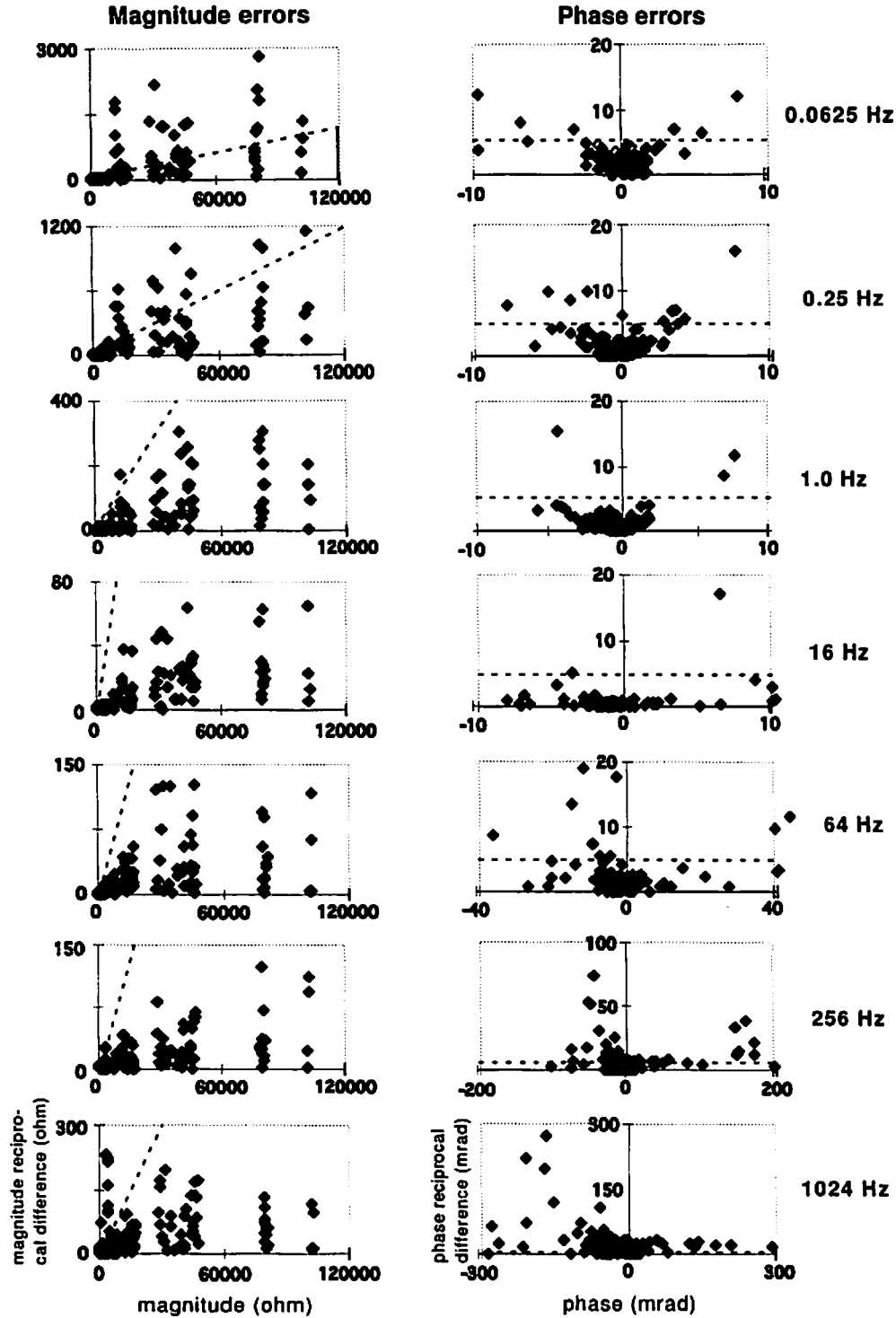


Figure 3. Measurement errors were estimated by comparing normal and reciprocal transfer impedances (magnitude and phase) for each of the 170 linearly independent measurements from the water blank model. The left column of plots shows the differences between each magnitude measurement and its reciprocal. These are plotted against the amplitude of the magnitude measurement (ohms). The right column of plots shows the differences between each phase measurement and its reciprocal; these differences are plotted against the amplitude of the phase measurement (milliradians). The sloped dashed line in the left column of plots delineates magnitude reciprocal differences equal to 1% of the measured magnitude. The horizontal dashed line in the right column of plots delineates phase reciprocal differences equal to 5 milliradians.

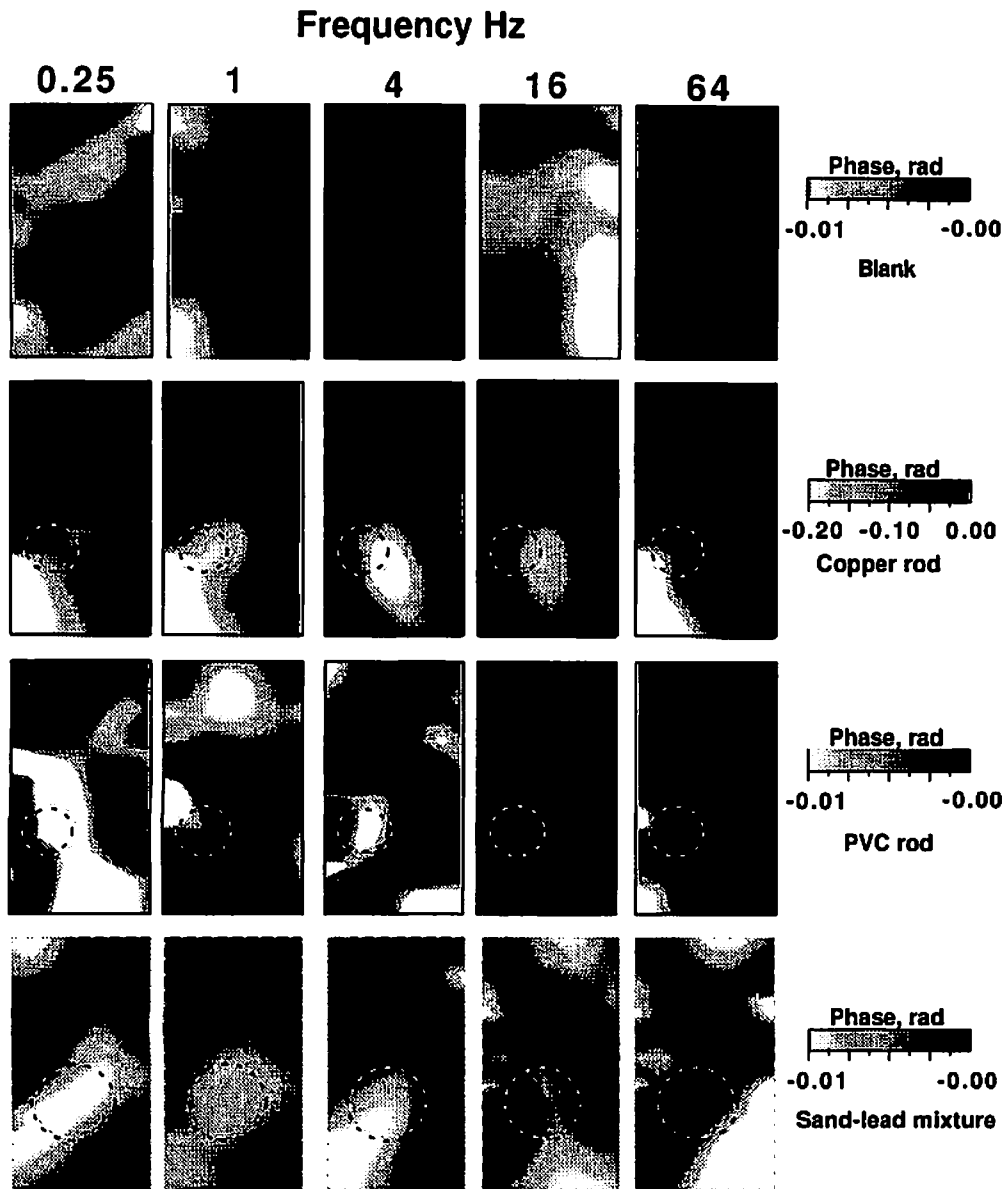


Figure 4. Impedance phase tomographs produced using the FE approach. The phase images are produced by comparing the magnitudes reconstructed for two frequencies (frequency effect) using the ERT algorithm. The tomographs show only the region between electrodes. This portion of the finite element mesh is 10 elements wide and 18 elements tall but each image is spatially smoothed. Notice that the grey scale bars are not all the same. The location and size of the targets are indicated by the dashed circles superimposed on the images.

obtained at 4 and 64 Hz, and the 64 Hz tomograph was calculated using the magnitudes obtained at 16 and 256 Hz.

Note that neither Eqs. 1 nor 2 enforce a negativity constraint on the phase. This means that with the FE approach, positive phase angles are possible even though such phases are unphysical at the low frequencies considered in this study. The PA and EIT methods enforce a negativity constraint on the phase. In order to use common gray scales to compare the FE, PA, and EIT phase tomographs, the

results in Fig. 4 are shown with any value greater than 0 set to the color black.

The top row of images in Fig. 4 shows the blank model results. Results for this model are images with phase angles ranging between 0 and 10 milliradians. Similar observations are made regarding the PVC rod images (third row of images in Fig. 4). Note that the blank and PVC rod images show phase anomalies which are not correlated with target location or magnitude, nor with frequency. We be-

lieve that these phase anomalies are probably caused by noise present in the resistivity images used to produce these results. These results indicate that the FE approach (as implemented here) cannot be used reliably to image targets with no IP response.

The copper rod phase images comprise the second row of images in Fig. 4. The location of the copper rod is indicated by the dashed circle superimposed on the images. Metallic objects are well known to create relatively large IP signals. The results for 4 and 16 Hz show a phase response near the target location with values ranging between 100 and 200 milliradians. The remaining frequencies show substantially distorted and poorly located phase anomalies.

The fourth row of images in Fig. 4 shows the FE phase anomalies for the sand-lead model; of all the models considered, this model should create the closest approximation to a natural geophysical system. The phase response created by the sand-lead target should be weaker than the copper rod response. The sand-lead images show values ranging between 0 and 20 milliradians. The 1 Hz image shows a phase response which is reasonably close to the target location and shape. Other frequencies show anomalies which are poorly detected and resolved.

Considering all the images together, it seems that the combined approach of using FE and resistivity images produced by an ERT algorithm cannot be used to dependably produce phase images. The method cannot resolve the copper rod reliably even though this model produces the largest phase anomalies. There is no systematic pattern in the location, size or amplitude for most of the FE reconstructions in Fig. 4.

Possible reasons for the poor performance observed may be: 1) the resistivity images are too noisy to accurately recover the relatively small changes generated by the FE, 2) the constant phase angle assumption inherent in the FE approach may be invalid for the targets used, 3) the resistivity images may be distorted because the ERT algorithm ignores the IP data when calculating the magnitude tomographs; thus, it does not model the potential fields correctly when polarizable targets are present, and 4) differences in the smoothness (parameter α in Eq. 4) applied to each tomograph cause incorrect changes in magnitude which are interpreted as phase delay.

Perturbation Analysis (PA)

The perturbation analysis uses the sensitivity matrix produced by an ERT algorithm to invert an approximate phase image consistent with the measured impedances. The results produced by this method are shown in Fig. 5. Because of the approximation used to calculate the phase, PA should be most reliable for small values of phase. The ERT algorithm used can produce images of magnitude and phase. However, the magnitude inversion is separate and disconnected from the IP inversion. Thus, the magnitude

inversion completely ignores the IP signals generated by polarizable targets. Also, this approach assumes that polarization is distributed throughout the volume and thus, the approximation should not apply to high conductivity targets (e.g., metallic objects) where surface polarization dominates the IP response (Siegel, 1959). As will be discussed later, this characteristic may degrade the resolution of magnitude tomographs obtained on polarizable targets.

First, we will discuss the magnitude reconstructions. ERT reconstructions of the water blank and PVC rod models are reasonable and behave as expected. The 32 ohm-m water is reconstructed as approximately 33 ohm-m. The resistive anomaly observed in the 1024 Hz image is likely due to the larger data errors at that frequency (see Fig. 3). While the PVC target is accurately located, its resistivity value is grossly underestimated in the reconstruction (the tomographs show 55 ohm-m magnitude whereas the resistivity for PVC plastic is above the MegaOhm-m range). This is a consequence of the smoothness constraint (Eq. 8) used to stabilize the algorithm. The resolution and sensitivity observed for both the copper and the sand-lead targets are worse than for the PVC target. Although a conducting anomaly appears above 0.125 Hz close to the copper target location, it is not well centered nor well formed. The sand-lead target is very poorly resolved, possibly because of the low electrical contrast with the water.

The PA phase reconstructions of the water blank target approximately yield the correct phase (0 milliradians). Notice that the phase images become sensitive to measurement noise at 64 Hz and above. For the copper rod and PVC rod models, the perturbation analysis produces images which are comparable to those from the EIT algorithm (Fig. 6). There is a considerable difference, however, for the sand-lead target where PA does a substantially poorer job of reconstructing either magnitude or phase. Apparently, for high contrast targets (i.e., copper rod magnitude and phase, and PVC rod magnitude) the perturbation analysis worked fairly well. Note that some of the PA assumptions are violated by the copper rod target; PA performance in this case was a pleasant surprise. On the other hand, when the magnitude or phase contrast was small (sand-lead target), this approximation performed relatively poorly. In the next section, it will be suggested that the EIT algorithm produces better magnitude and phase images (at least below 256 Hz) for the various targets.

Comparison of ERT and EIT Tomographs

In order to compare the FE and PA images with the EIT images, it is necessary to first examine the resistivity inversions performed by the ERT algorithm used by the PA approach (the magnitude plots in Fig. 5). For the uniform resistivity case (water blank) the ERT images are approximately uniform at about 32 ohm-m at all frequencies except 1024 Hz. The ERT approach is also able to image well the

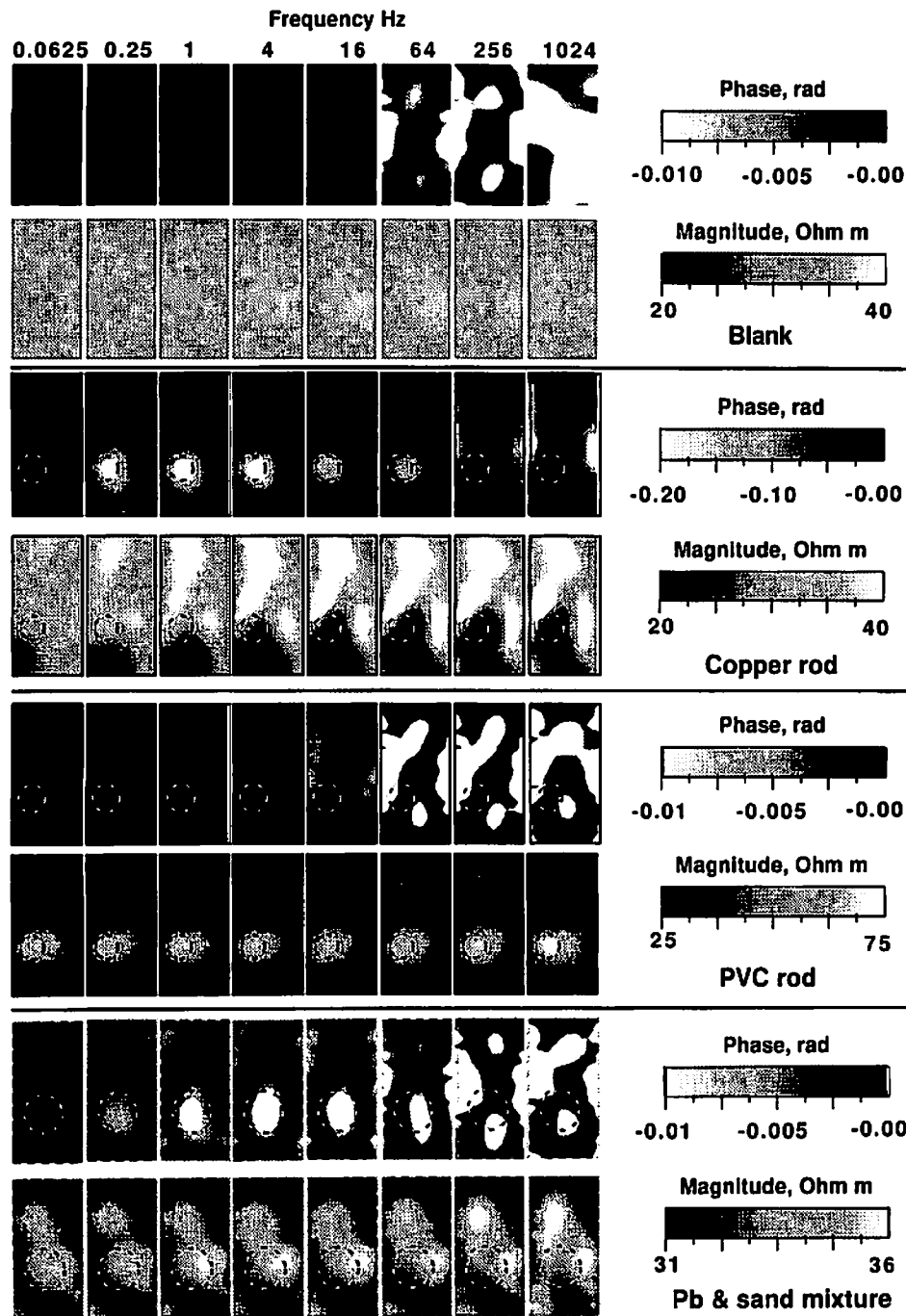


Figure 5. Impedance magnitude and phase using the linearized perturbation analysis approach. Finite element mesh details are as indicated in the Fig. 4 caption.

position of the high contrast resistive model (PVC rod target) although it yields a low estimate (only 55 ohm-m reconstructed while the resistivity of PVC is above the MegaOhm-m range) for its magnitude. We should expect a poor reconstruction for a high contrast target since the code is stabilized with a spatially smooth, Occam's type inversion. The smoothing has the effect of smearing the anomaly

and reducing its contrast. For the highly conducting, copper rod target, the ERT algorithm performs poorly, having trouble even locating the target position. If this problem were just one of high contrast then the result should improve for the intermediate resistivity contrast case provided by the sand-lead target. However, the sand-lead target is also poorly resolved when phase information is ignored. These ob-

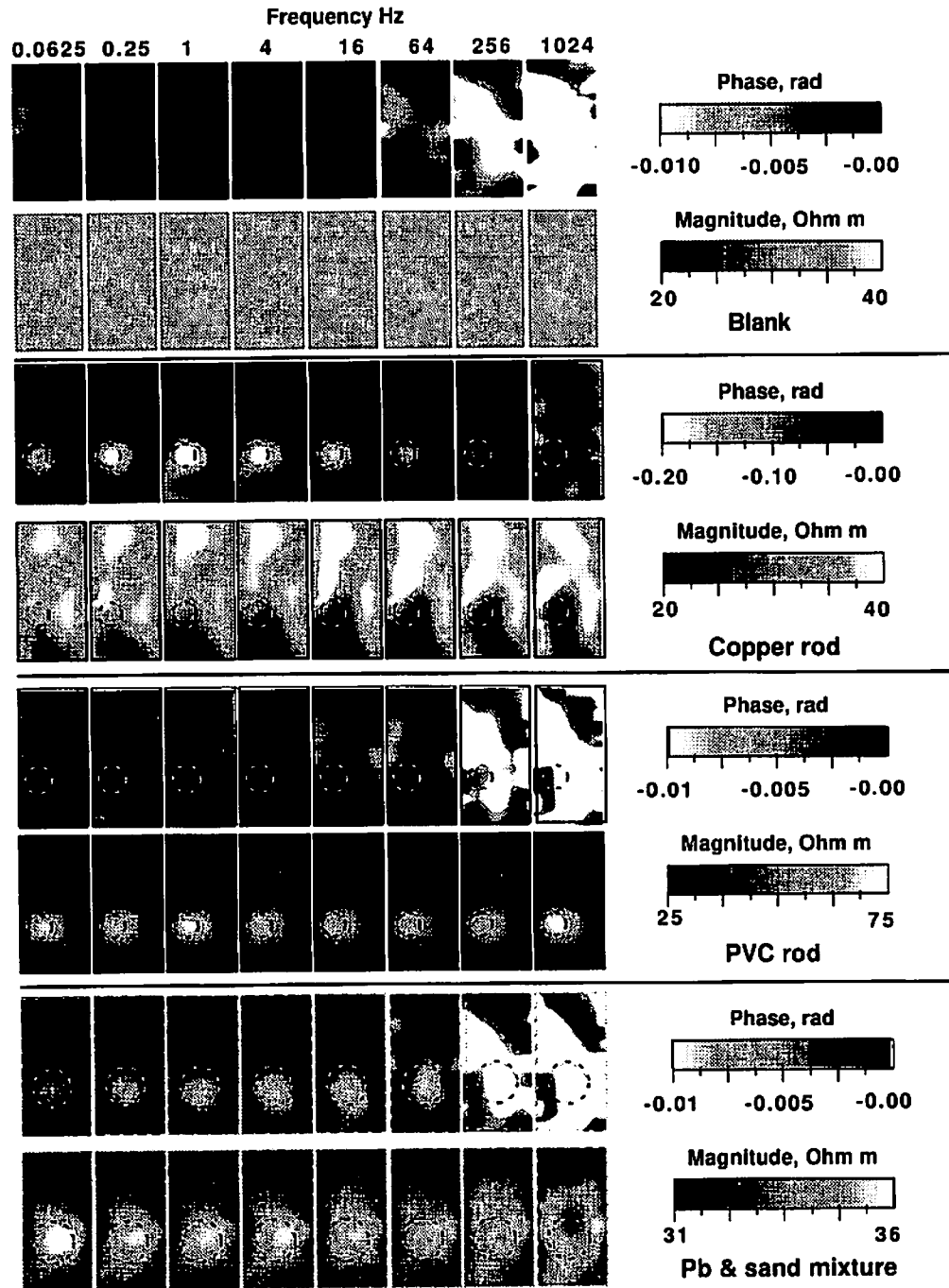


Figure 6. Impedance magnitude and phase using the EIT approach. Other image details are as indicated in the Fig. 4 caption.

servations suggest that impedance magnitude is reconstructed poorly when the target has a significant IP response and the IP data is ignored by the inversion algorithm.

Let us now compare the magnitude inversions which ignore IP data (ERT), with the magnitude inversions in Fig. 6, where the reactive effects are included (EIT). These comparisons will help define what, if anything, has been gained by rigorously accounting for the reactance while calculating

the magnitude tomographs. Both ERT and EIT yield nearly uniform 30 ohm-m images of the water blank target, for all frequencies. Similarly, the PVC target's location, size, and contrast relative are rendered equally well by the EIT and ERT algorithms.

The EIT and ERT magnitude inversions of the copper rod target are disappointing, both methods showing relatively poor spatial resolution. The reason(s) for the poor

performance are not fully understood although a conductive target in a relatively conductive medium is clearly more difficult to detect than a resistive target. Figures 5 and 6 indicate that spatial resolution and resistivity contrast of the copper rod improves with increasing frequency. We also observed that the measured transfer resistances for the raw copper rod decreased with increasing frequency. Data from the other targets did not show this trend, thereby suggesting that the frequency dependent magnitudes are caused by decreases in contact impedance at the metal-electrolyte interface as the frequency increases. These results suggest that the spatial resolution of metallic objects in magnitude images can be improved by going to higher frequencies.

Surprising results are observed in the magnitude tomographs for the intermediate resistivity sand-lead target; this target creates conditions which are most similar to those encountered during field surveys. EIT magnitude inversions produced a well defined weakly resistive anomaly of 35 ohm-m at 0.06265 Hz which decreased to about 32 ohm-m at 16 Hz. Although it is positioned too close to the image center, there is no doubt that approximate target shape, size and location are evident; the same cannot be said for the tomographs recovered when the reactive effects were ignored (Fig. 5 magnitude reconstructed by the ERT algorithm). The complex algebra algorithm (EIT) appears superior to the algorithm using only real algebra (ERT) based strictly on comparisons of magnitude inversions. The sand-lead model results suggest that, when the reconstruction algorithms make proper use of the IP data, better magnitude reconstructions may be achieved.

Now let us consider any other possible benefits which may arise from inverting phase with an EIT algorithm. Both the water blank and the PVC targets should have no reactive component at these frequencies given that there is no known mechanism for generating an IP signal. Except for the tomographs corresponding to higher frequencies, which are undoubtedly corrupted by data errors, we find that the phase images for both targets are less than about 10 milliradians. Although they are plotted to different scales we can see that below 256 Hz the reconstructed phases are less than about 5 milliradians but are double that at 256 and 1024 Hz. This is consistent with Fig. 3 which clearly shows a much higher measured phase error at these two frequencies. The reconstructed phase values are therefore likely caused by these measurement errors propagating through the inversion algorithm. Images of the water blank serve to illustrate the effects of measurement error in the phase reconstructions of other targets. The error bounds inferred from these results are: 5 milliradians below 256 Hz and 10 milliradians at 256 and 1024 Hz.

We now consider the phase reconstruction for the copper rod target. Although we do not know what phase amplitude should be reconstructed for this target, the copper-electrolyte interface should produce a significant IP re-

sponse. At all but the highest frequencies, the copper rod target is accurately located and is reconstructed as a capacitive reactance. A key observation is that the phase tomographs yield a more faithful representation of the target shape, location, and size than do the magnitude tomographs. These results reinforce the suggestion that inversion of impedances (EIT) provide better resolution than inversion of resistance (ERT).

An equally important conclusion comes from the phase images of the sand-lead target. In this case, the phase response is about one twentieth that of the copper rod target, and it is above the noise level at frequencies below 256 Hz. Even more important is that the target was not clearly imaged by the ERT algorithm, but both the magnitude and phase reconstructions of EIT show the anomaly. These results indicate that measuring and inverting both the resistive and reactive portions of the earth response can help delineate targets better than what is possible with the resistive portion only. We suspect that this improvement results from additional target information contained in the IP data which serves as an additional constraint during minimization of the objective function (see Eq. 18).

The results from these tests consider only a limited range of experimental conditions and need verification under a wider range of conditions. Nevertheless, we suggest that the use of an EIT algorithm may be desirable because of the observed improvement in spatial resolution, even if the IP response is of no direct interest.

Summary and Conclusions

We have used and evaluated three different methods for reconstructing images of electrical impedance from measurements of impedance magnitude and phase: frequency effect (FE), perturbation analysis (PA), and electrical impedance tomography (EIT, a generalization of ERT). We chose to compare these methods using data from four bench scale physical models: a uniform target with no IP response, a highly conductive target with a large IP response, a highly resistive target with no IP response and a low contrast conductive target with a small IP response. Impedance magnitude and phase were reconstructed using the data collected.

For all targets, the FE method as implemented here did not produce reliable images of phase. Possible reasons for the poor performance are that the resistivity images are too noisy to accurately recover the relatively small changes in generated by the FE, and that the constant phase angle assumption inherent in the FE approach may be invalid for the targets used.

The EIT and PA algorithms provided useful magnitude and phase images for the frequency range of 0.0625 to 64 Hz; images for higher frequencies were not reliable. The EIT magnitude images showed noticeably better spatial

resolution than the PA magnitude images for the sand-lead target (small IP response). For other targets, the magnitude images from both methods were very similar. The EIT and PA magnitude tomographs for the copper rod target indicate that spatial resolution improved with increasing frequency. We believe that this behavior is indicative of decreasing capacitive reactance at the metal-electrolyte boundary with increasing frequency. The copper rod results suggest that the spatial resolution for metallic objects observed in magnitude images can be improved by going to higher frequencies.

Phase images from both methods provided better spatial resolution than the magnitude images for targets displaying an IP response (copper rod, and sand-lead mixture). EIT and PA phase images represented well the location and shape of the IP targets. However, we were unable to verify the accuracy of the reconstructed phase values. The EIT phase images showed better spatial resolution than the PA phase images for the sand-lead target, which is the model that most closely resembles a natural geophysical system. This may result from an added constraint in the EIT algorithm objective function as a result of additional information contained in the IP data.

When the IP signal was clearly absent in the target, EIT and PA reconstructed phase values less than a few milliradians, the noise level of the raw data. Considering the computational efficiency of the PA method, the results may be considered acceptable.

IP data has traditionally been used to discriminate between types of geologic materials, *e.g.*, location of an ore body within a larger mass of rock. The magnitude and phase images presented here suggest that IP data can provide additional value. When IP data are inverted, phase tomographs show better spatial resolution than magnitude tomographs. Also, the magnitude tomographs of some IP targets may show improved spatial resolution when the IP data are inverted using an EIT algorithm. We also believe that these results need to be validated under a wider set of conditions. Based on these observations, we suggest that the use of an EIT algorithm is desirable even when the IP response is of no direct interest.

Acknowledgments

We acknowledge helpful contributions from Andreas Kemna, D.D. (Skip) Snyder, R. Staley, and K. Zonge which contributed to the success of this work. This work was performed under the Earth and Environmental Sciences Directorate at LLNL. It was funded by the Characterization, Monitoring and Sensors Technology Program, Office of Technology Development, U.S. Department of Energy (DOE). Work performed under the auspices of the U.S. Department of Energy by Lawrence Livermore National Laboratory under Contract W-7405-ENG-48.

References

- Barber, D.C., and Seagar, A.D., 1998, Fast reconstruction of resistance images: *Clinical Physics and Physiological Measurement*, 8, Suppl. A, 47–55.
- Bard, Y., 1974, *Nonlinear parameter estimation*: Academic Press, pp. 111–113.
- Bertin, J., and Loeb, J., 1976, *Experimental and theoretical aspects of induced polarization*: Vol. 1 and 2, Gebruder Borntraege.
- Borner, F., Gruhne, M., and Schon, J., 1993, Contamination indications derived from electrical properties in the low frequency range: *Geophysical Prospecting*, 41, 83–98.
- Considine, D.M., 1983, *Van Nostrand's Scientific Encyclopedia*: Van Nostrand Reinhold Company, New York.
- Daily, W., and Owen, E., 1991, Cross-borehole resistivity tomography: *Geophysics*, 56, 1228–1235.
- Daily, W.D., Ramirez, A., and Johnson, R., 1998, Electrical impedance tomography of a perchloroethylene release: *J. Environ. and Eng. Geophysics*, 2, 189–201.
- Dines, K.A., and Lytle, R.J., 1981, Analysis of electrical conductivity imaging: *Geophysics*, 46, 1025–1036.
- deGroot-Hedlin, C., and Constable, S., 1990, Occam's inversion to generate smooth, two-dimensional models from magnetotelluric data: *Geophysics*, 55, 1613–1624.
- Ellis, R.G., and Oldenburg, D.W., 1997, The pole pole 3D DC resistivity inverse problem—a conjugate gradient approach: *Geophysical Journal International*, 119, 187–194.
- Henderson, R.P., and Webster, J.G., 1978, An impedance camera for spatially specific measurements of thorax: *IEEE Trans. Biomed. Eng.* BME-25, 250–254.
- Iwatate, D.F., Narbutovskih, S.M., Sweeney, M.D., Daily, W., Ramirez, A.L., Morey, R.M., and Christensen, L., 1996, Feasibility of CPT-deployed vertical electrode array in single-shell tank farms: WHC-SD-EN-TA-004, Rev. 0.
- Kemna, A., and Binley, A., 1996, Complex Electrical Resistivity Tomography for Contaminant Plume Delineation, *in Proc. 2nd Meeting of the Environmental and Engineering Geophysics Society*, Nantes, 2–5 September, pp. 96–199.
- LaBrecque, D., Schima, S., and Lundegard, P., 1994, The use of cross-borehole IP to monitor unsaturated flow, *in Proc. John S. Sumner Memorial International Workshop on Induced Polarization in Mining and the Environment*, University of Arizona, Tucson, AZ, Oct. 17–20.
- LaBrecque, D.J., Miletto, M., Daily, W., Ramirez, A., and Owen, E., 1996a, The effects of noise on Occam's inversion of resistivity tomography data: *Geophysics*, 61, 538–548.
- LaBrecque, D.J., Ramirez, A., Daily, W., Binley, A., and Schima, S., 1996b, ERT monitoring of environmental remediation processes: *Meas. Sci. Technol.*, 7, 375–383.
- Lytle, R.J., and Dines, K.A., 1978, An impedance camera: A system for determining the spatial variation of electrical conductivity: Lawrence Livermore Laboratory, Livermore, California, UCRL-52413.
- Marshall, D.J., and Madden, T.R., 1959, Induced polarization, a study of its causes: *Geophysics*, 24, 790–816.
- Olhoeft, G.R., 1985, Low-frequency electrical properties: *Geophysics*, 50, 2492–2503.

- Oldenburg, D.W., and Li, Y., 1994, Inversion of induced polarization data: *Geophysics*, **59**, 1327–1341.
- Pelton, W.H., Rijo, L., and Swift Jr., C.M., 1978, Inversion of two-dimensional resistivity and induced-polarization data: *Geophysics*, **43**, 788–803.
- Pelton, W., Sill, W., and Smith, B., 1983, Interpretation of complex resistivity and dielectric data, Part I: *Geophysical Transactions*, **29**, 297–330.
- Pelton, W., Sill, W., and Smith, B., 1984, Interpretation of complex resistivity and dielectric data, Part II: *Geophysical Transactions*, **30**, 11–45.
- Press, W.H., Flannery, B.P., Teukolsky, S.A., and Vetterling, W.T., 1986, *Numerical recipes*: Cambridge University Press.
- Ramirez, A., Daily, W., and R. Newmark, 1995, Electrical resistance tomography for steam injection and process control: *J. Environmental and Engineering Geophysics*, **0**, 39–51.
- Ramirez, A., Daily, W., Binley, A., LaBrecque, D., and Roelant, D., 1996, Detection of leaks in underground storage tanks using electrical resistance methods: *J. Environmental and Engineering Geophysics*, **1**, 189–203.
- Sasaki, Y., 1992, Resolution of resistivity tomography inferred from numerical simulation: *Geophysical Prospecting*, **40**, 453–463.
- Shi, W., Rodi, W., Mackie, R., and Zhang, J., 1996, Electrical resistivity inversion with application to a contamination site in the Aberjona watershed, *in Proc. of Symposium on the Application of Geophysics to Engineering and Environmental Problems*, Keystone, CO, Apr. 28–May 2, pp. 1257–1268.
- Shi, W., Rodi, W., and Morgan, F.D., 1998, 3D induced polarization inversion using complex electrical resistivities, *in Proc. of Symposium on the Application of Geophysics to Engineering and Environmental Problems*, Chicago, Mar. 22–26, pp. 785–794.
- Shuey, R.T., and Johnson, M., 1973, On the phenomenology of electrical relaxation in rocks: *Geophysics*, **38**, 37–48.
- Siegel, H.O., 1959, Mathematical formulation and type curves for induced polarization: *Geophysics*, **24**, 547–565.
- Sumner, J.S., 1976, *Principles of induced polarization for geophysical exploration*: Science Publ. Co.
- Tikhonov, A.N., and Arsenin, V.Y., 1977, *Solutions of ill-posed problems*: V.H. Winston and Sons.
- Tripp, A.C., Hohmann, G.W., and Swift, C.M., 1984, Two dimensional resistivity inversion: *Geophysics*, **49**, 1708–1717.
- Vanhala, H., Soininen, H., and Kukkonen, I., 1992, Detecting organic chemical contaminants by spectral-induced polarization method in glacial till environment: *Geophysics*, **57**, 1014–1017.
- Van Voorhis, G.C., Nelson, P.H., and Drake, T.L., 1973, Complex resistivity spectra of porphyry copper mineralization: *Geophysics*, **38**, 49.
- Vinegar, H.J., and Waxman, M.H., 1984, Induced polarization of shaly sands: *Geophysics*, **49**, 1267–1287.
- Weller, A., Seichter, M., and Kampke, A., 1996, Induced polarization modelling using complex electrical conductivities: *Geophysical Journal International*, **127**, 387–398.
- Wexler, A., Fry, B., and Neuman, M.R., 1985, Impedance-computed tomography algorithm and system: *Applied Optics*, **24**, 3985–3992.
- Wynn, J.C., and Zonge, K.L., 1975, EM coupling, its intrinsic value, its removal and the cultural coupling problem: *Geophysics*, **40**, 831–850.
- Yorkey, T.J., Webster, J.G., and Tompkins, W.J., 1987, Comparing reconstruction algorithms for electrical impedance tomography: *IEEE Trans Biomedical Engineering*, **BME-34**, 843–852, November.
- Yuval, and Oldenberg, D.W., 1997, Computation of Cole-Cole parameters using IP data: *Geophysics*, **62**, 436–448.
- Zhang, J., Mackie, R.L., and Madden, T.R., 1995, 3-D resistivity forward modelling and inversion using conjugate gradients: *Geophysics*, **60**, 1313–1325.
- Zonge, K.L., and Wynn, J.C., 1975, Recent advances and applications in complex resistivity measurements: *Geophysics*, **40**, 851–864.